Energetic Neutral Atom Distribution on the Lunar Surface and Its Relationship with Solar Wind Conditions

H. Z. Wang[1,2] , C. Xiao[1,2] , Q. Q. Shi[1,2] , R. L. Guo[1,2] , C. Yue[3] , L. H. Xie[2] , J. Zhang[1] , A. B. Zhang[4,5] ,
M. Wieser[6] , Y. Saito[7] , M. N. Nishino[5] , M. Nowada[1] , Q. G. Zong[3] , A. W. Degeling[1] , A. M. Tian[1] , S. Y. Fu[3] ,
H. Zhang[8] , J. Chen[1] , T. X. Zhang[8] , J. Liu[2] , C. Y. Han[2] , W. S. Shang[1] , and S. C. Bai[1]

[1] Laboratory of Optical Astronomy and Solar-Terrestrial Environment, School of Space Science and Physics, Institute of Space Sciences, Shandong University, Weihai, Shandong, 264209, People's Republic of China; sqq@sdu.edu.cn, zhang_jiang@sdu.edu.cn
[2] State Key Laboratory of Space Weather, National Space Science Center (NSSC), Chinese Academy of Sciences, Beijing, People's Republic of China
[3] School of Earth and Space Sciences, Peking University, Beijing, People's Republic of China
[4] Beijing Key Laboratory of Space Environment Exploration, National Space Science Center, Chinese Academy of Sciences, Beijing, People's Republic of China
[5] University of Chinese Academy of Sciences, Beijing, People's Republic of China
[6] Swedish Institute of Space Physics, Kiruna, Sweden
[7] Institute of Space and Astronautical Science, Japan Aerospace Exploration Agency, 3-1-1 Yoshinodai, Chuo-ku, Sagamihara, Kanagawa 252-5210, Japan
[8] Key Laboratory of Earth and Planetary Physics, Institute of Geology and Geophysics, Chinese Academy of Sciences, Beijing, People's Republic of China
Received 2021 July 23; revised 2021 October 27; accepted 2021 October 28; published 2021 December 2

Abstract

The Advanced Small Analyzer for Neutrals (ASAN) on board the Chang'E-4 Yutu-2 rover first detected energetic neutral atoms (ENAs) originating from the lunar surface at various lunar local times on the lunar farside. In this work, we examine the ENA energy spectra, obtained in the first 23 lunar days from 2019 January 11 to 2020 October 12, and find a higher ENA differential flux on the lunar dawnside than on the duskside. Combined with Acceleration, Reconnection, Turbulence and Electrodynamics of the Moon's Interaction with the Sun (ARTEMIS) data, we analyze the correlation between the ENA differential flux and solar wind parameters, such as flux, density, dynamic pressure, and velocity, for each ASAN energy channel on the dawnside and duskside. The results show that ENA differential flux is positively correlated with solar wind flux, density, and dynamic pressure and relatively lower on the duskside than on the dawnside. To determine the relationship between solar wind energy and ENA energy, we analyze the correlation between solar wind energy and ENA cutoff energy and temperature on the dawnside and duskside. The results show that the ENA cutoff energy and temperature are lower on the duskside than on the dawnside at the same solar wind energy. The difference between the ENA–solar wind observation on the dawnside and duskside is possibly caused by solar wind deflection and deceleration on the duskside, which can be attributed to the interaction between solar wind and the lunar magnetic anomalies located nearby in the northwestern direction of the Chang'E-4 landing site.

Unified Astronomy Thesaurus concepts: Solar wind (1534); Lunar surface (974); Space plasmas (1544); The Moon (1692)

1. Introduction

The lunar surface is exposed to solar wind protons due to a lack of a global magnetic field or dense atmosphere. The interactions between the solar wind and lunar surface have been investigated for several decades. Although most of the solar wind protons are neutralized when impacting on the lunar surface (Crider & Vondrak 2002), the in situ observations from Chang'E, Kaguya, Chandrayaan-1, and Interstellar Boundary Explorer (IBEX) missions reveal that 0.1%–1% of solar wind protons are backscattered from the lunar surface (Saito et al. 2008; Wang et al. 2010), 10%–20% are converted to energetic neutral atoms (ENAs; McComas et al. 2009; Wieser et al. 2009), and the remaining part are implanted into the lunar regolith to produce OH/H_2O, as previously found for nonmagnetized regions of the surface (Li & Garrick-Bethell 2019; Wang et al. 2021). The reflection ratio would be much higher over large-scale regions of magnetic anomalies (average ∼10%, locally ∼50%; Saito et al. 2010; Lue et al. 2011). Among these

processes, measurement of ENAs is considered to be one of the best ways to provide useful information on the interactions between the solar wind protons and the lunar surface, such as the surface composition and the location and strength of magnetic anomalies (localized regions of strong crustal magnetization with surface magnetic field strengths on the order of tens to hundreds of nT; Futaana et al. 2006).

The observations of ENAs have been made under different plasma conditions (solar wind, the Earth's magnetosheath, and the Earth's plasma sheet) and lunar regions (e.g., magnetic anomalies) from ENA instruments on board the IBEX and Chandrayaan-1 missions (Futaana et al. 2006). During about three-quarters of the lunar orbit, the Moon is immersed in the solar wind that provides a predominant proton flux at around 1 keV and a typical speed of about 400 km s^{-1}. However, when the Moon enters into the Earth's magnetosheath and plasma sheet, the plasma density, temperature, and Mach numbers of the space environment around the Moon differ significantly from those in the solar wind. When the Moon is in the undisturbed solar wind, the intensity of the reflected neutral atom flux changes corresponding with the solar wind incident angle and the intensity of the solar wind proton flux (Wieser et al. 2009). The scattering function of backscattered ENAs was derived using the Chandrayaan-1 Energetic Neutral Atom
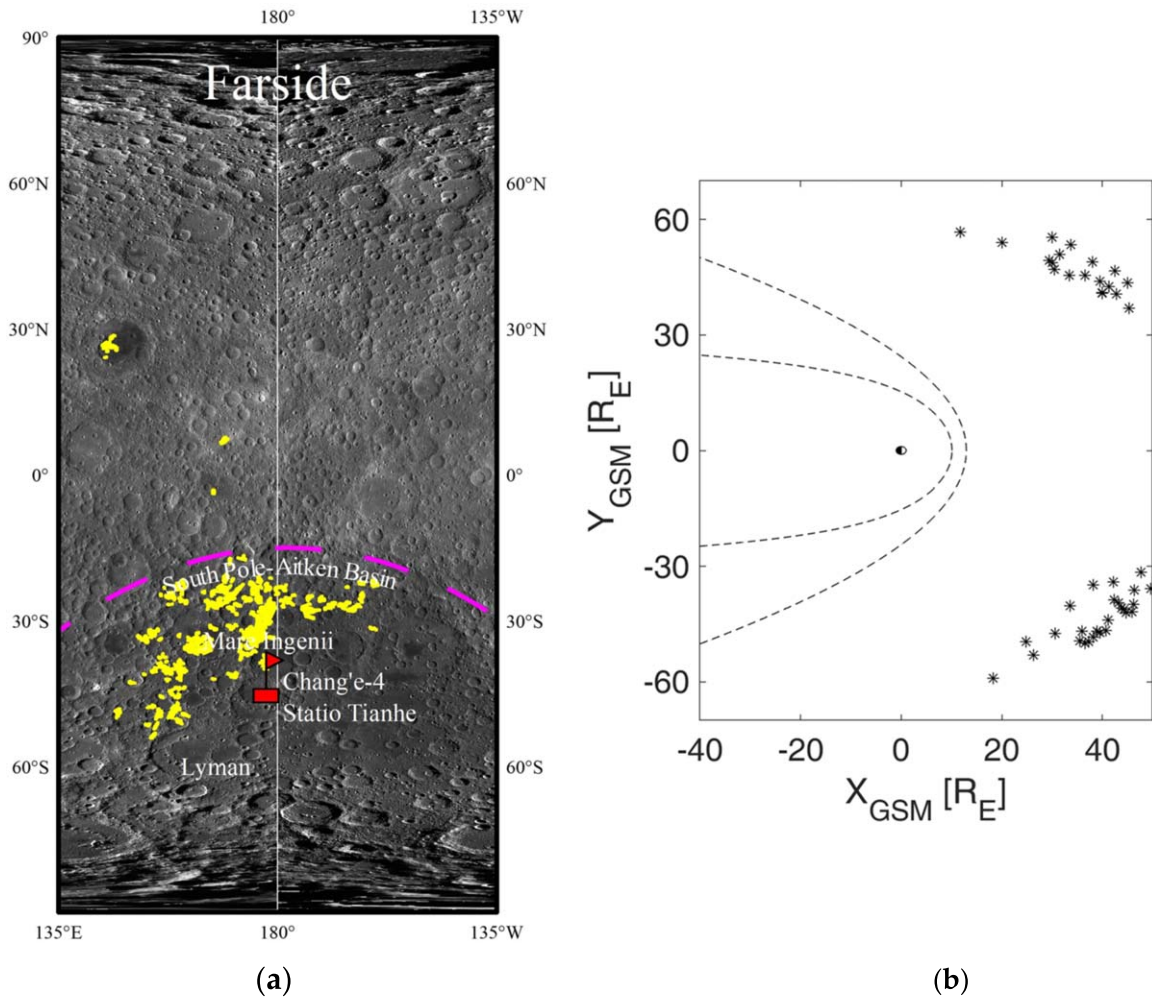
Figure 1. (a) Chang'E-4 landing site in the selenography coordinate system (overlaid on the Lunar Reconnaissance Orbiter Wide Angle Camera base map). The yellow area indicates the magnetic anomaly region. The magenta dashed line indicates the boundary of the South Pole-Aitken basin. (b) Overview of the ARTEMIS positions in the GSM coordinate system during the operation of ASAN, along with typical boundaries for the terrestrial bow shock (Fairfield 1971) and magnetopause (Shue et al. 1997).

(CENA) data, and it is also used to map a global solar wind reflection ratio from the lunar surface (Schaufelberger et al. 2011; Vorburger et al. 2013). A reduced ENA flux is observed above the magnetic anomalies, which indicates a local ion shielding effect (Wieser et al. 2010; Vorburger et al. 2012). The shielding efficiencies depend on the magnetic field strength, the geometric structure of the magnetic anomalies, and the solar wind dynamic pressure (Wieser et al. 2010; Vorburger et al. 2012). Allegrini et al. (2013) compared the ENA energy spectra in the Earth's magnetosheath observed by IBEX and found that the ENA intensities are generally higher in the magnetosheath. However, Lue et al. (2016) found that the ENA scattering process remains unchanged in Earth's magnetosheath compared with the undisturbed solar wind condition from the Chandrayaan-1 ENA measurements. They also observed the shielding effect of magnetic anomalies in the magnetosheath. When the Moon enters into the Earth's magnetotail, the solar wind is shielded by Earth's magnetic field; however, the energy of protons in the plasma sheet is higher, even though the proton flux is reduced compared with the solar wind proton flux. Harada et al. (2014) found that the plasma sheet protons can also be scattered as ENAs from the lunar surface, and magnetic shielding of the lunar surface is less effective than in the solar

wind due to the broad velocity distributions of the plasma sheet protons. The solar wind conditions vary dynamically, with significant variations in parameters such as the solar wind velocity, proton density, and proton flux. Futaana et al. (2012) found a good correlation between the solar wind velocity and the temperature of the ENAs. Funsten et al. (2013) found that the ENA reflection coefficient exhibits a strong dependence on the incident solar wind speed.

These orbital observations promote our understanding of the interactions between the plasma and the lunar surface. However, studies of ENAs based on in situ observations on the lunar surface had not been conducted until the Chang'E-4 mission.

The Advanced Small Analyzer for Neutrals (ASAN) on board the Chang'E-4 Yutu-2 rover achieved the first in situ observation of ENAs on the lunar surface. Chang'E-4 landed on the lunar farside surface on 2019 January 3 at 177°.6 E, 45°.5 S within the South Pole-Aitken basin (Di et al. 2019; Liu et al. 2019; Wu et al. 2019; Liu et al. 2020; Wieser et al. 2020), as shown in Figure 1(a). The South Pole-Aitken basin is the largest confirmed impact basin of the Moon; it has unusual surface properties, such as a low albedo, and coincides with a cluster of strong magnetic anomalies located on the northern

rim of the basin. Vorburger et al. (2015) studied ENA observations in the South Pole-Aitken basin and tried to find a correlation between the ENA map and local surface features. However, they only found ENA depletion at the magnetic anomalies in the South Pole-Aitken basin and no correlation with elevation, albedo, or compositions (iron and thorium) using the total ENA flux data. The dependence of the ENA spectra on surface properties remains unclear because the observation's geometry area was large. Zhang et al. (2020) presented the first result of ASAN and found that the reflection ratio derived from ASAN data has a good agreement with previous works from the Chandrayaan-1 and IBEX missions. However, the influence of the variation of the ENA spectra on the lunar surface with solar wind parameters remains unclear. In the present work, we study the ENA distribution and the relationship between the ENA differential flux and solar wind parameters from Acceleration, Reconnection, Turbulence and Electrodynamics of the Moon's Interaction with the Sun (ARTEMIS) observations, such as flux, density, velocity, and dynamic pressure.

This paper consists of five sections. The introduction and background of this study are described in Section 1. Section 2 provides a brief description of the ARTEMIS and Chang'E-4 ASAN data used in this study. In Section 3, we present the main results obtained through this study: ENA observations over 17 lunar days, the statistical correlation between lunar ENA differential flux and solar wind parameters, and the relationship between the solar wind energy and ENA cutoff energy on the dawnside and duskside. In Section 4, we discuss significant features of the statistical results and physics obtained from our statistical study. Finally, the major conclusions of this paper are provided in Section 5.

2. Data and Methods

2.1. ASAN Instrument

The ASAN on board the Chang'E-4 Yutu-2 rover is an energetic neutral analyzer, whose energy range is from 10 eV to 10 keV with typically 30% energy resolution (Wieser et al. 2020). The field of view is a single angular pixel of $37° \times 30°$ pointing at the lunar surface. Figure 1(b) shows the lunar positions (all in the solar wind) in the Geocentric Solar Magnetospheric (GSM) coordinate system when the ASAN is operated. The ASAN was powered on aperiodically for tens of minutes, on average, in two operation windows during each lunar day, one during the local morning from 07:00 to 09:00 lunar local time and the other during the local afternoon from 14:00 to 16:00 lunar local time (Figure A1(a)). We use the data from 2019 January 11 to 2020 April 28, a total of 54 intervals of ENA data over 23 lunar days. In these operations, 31 observations are in the local morning, and 23 observations are in the local afternoon. The observation geometries (solar azimuth angle, solar zenith angle, solar elevation angle, solar elevation angle of rover, solar azimuth angle of rover) during each operation, along with the lunar local time, are shown in Figures A1(b)–(f). The definitions of these angles are shown in the Appendix. In this study, we only used the hydrogen ENA data as shown in Figure A1(g).

2.2. ARTEMIS Data

The ARTEMIS probes were originally part of the five Time History of Events and Macroscale Interactions during

Substorms (THEMIS) spacecraft in the near-Earth magnetosphere. In early 2010, they gradually started to move outward to their final orbits at the lunar distances of 60 Earth radii (RE). The ARTEMIS mission consists of a pair of identically instrumented spacecraft that have been in orbit around the Moon since mid-2011 (Angelopoulos 2011; Sibeck et al. 2011). Both probes measure in situ low-energy ion (up to 25 keV) and electron (up to 30 keV) distributions with an electrostatic analyzer (ESA; McFadden et al. 2008). In this study, we used the ion measurements from the two ARTEMIS probes (ARTEMIS-P1 and ARTEMIS-P2) to study the variation of the lunar plasma environment during the observation times of the Chang'E-4 ASAN instrument. The mean values of the solar wind velocity, density, pressure, and ion flux obtained from ARTEMIS during each ASAN operation event are shown in Figures A1(h)–(k). The solar wind energy was calculated by $E_{sw} = 0.5^*(1.6^*10^{-27})^*(V_{sw}^*10^3)^2/(1.6^*10^{19})$.

3. Observations

An overview of the ENA energy spectra distribution during the first 23 lunar days is shown in Figure 2. As we mentioned in previous sections, the operation time of ASAN is aperiodic, which means that ENAs are not always measured on both dawnside and duskside in each lunar day (e.g., not on the 1st, 9th, and 15th lunar days). However, based on the 17 lunar days with both dawnside and duskside measurements, we find that the ENA differential flux is higher on the dawnside, except on the 12th lunar day. The solar wind parameters and the ENA integral flux on the dawnside and duskside in each lunar day are shown in Figure A2. From previous studies, we know that the intensity of the ENA flux varies with the solar wind incident angle and the intensity of the solar wind proton flux (Wieser et al. 2009). Here we find that the ENA fluxes obtained on the duskside are generally lower than those on the dawnside, even though the intensity of the solar wind flux is higher on the duskside with similar solar elevation angles, such as on the 7th, 13th, 16th, 20th, 21st, and 22nd lunar days. Comparing the 12th and 13th lunar days in Figures 2 and A2, we can find that the ENA differential flux is higher on the duskside than on the dawnside if both the solar wind flux and dynamic pressure are higher on the duskside. When the ASAN operates on the lunar duskside, the solar wind protons are coming from the northwestern direction, passing through the magnetic anomalies in the South Pole-Aitken basin (yellow points in Figure 1(a)). During the ASAN operation on the dawnside, the solar wind protons are coming from the northeastern direction, in which there are few magnetic anomalies.

Statistics of the correlation between the ENA differential flux and the solar wind integrated flux at each ASAN energy channel on both the dawnside and duskside are shown in Figure 3. The data were removed when the ENA differential flux was less than the data sensitivity limit line. First, from the statistical result between the ENA differential flux and the solar wind flux, we can find that the ENA differential flux has a positive correlation with the solar wind flux on both the dawnside and duskside, which is consistent with previous studies (Wieser et al. 2009). The linear fitting results of Figure 3 are shown in Table A1 ($df_{ENA} = c^*f_{SW} + k$), where c represents the reflection coefficient. A positive k could indicate that there is another source. There are also few negative k values in the table, as the data set might not be large enough. The correlation coefficient is higher at ENA energies between
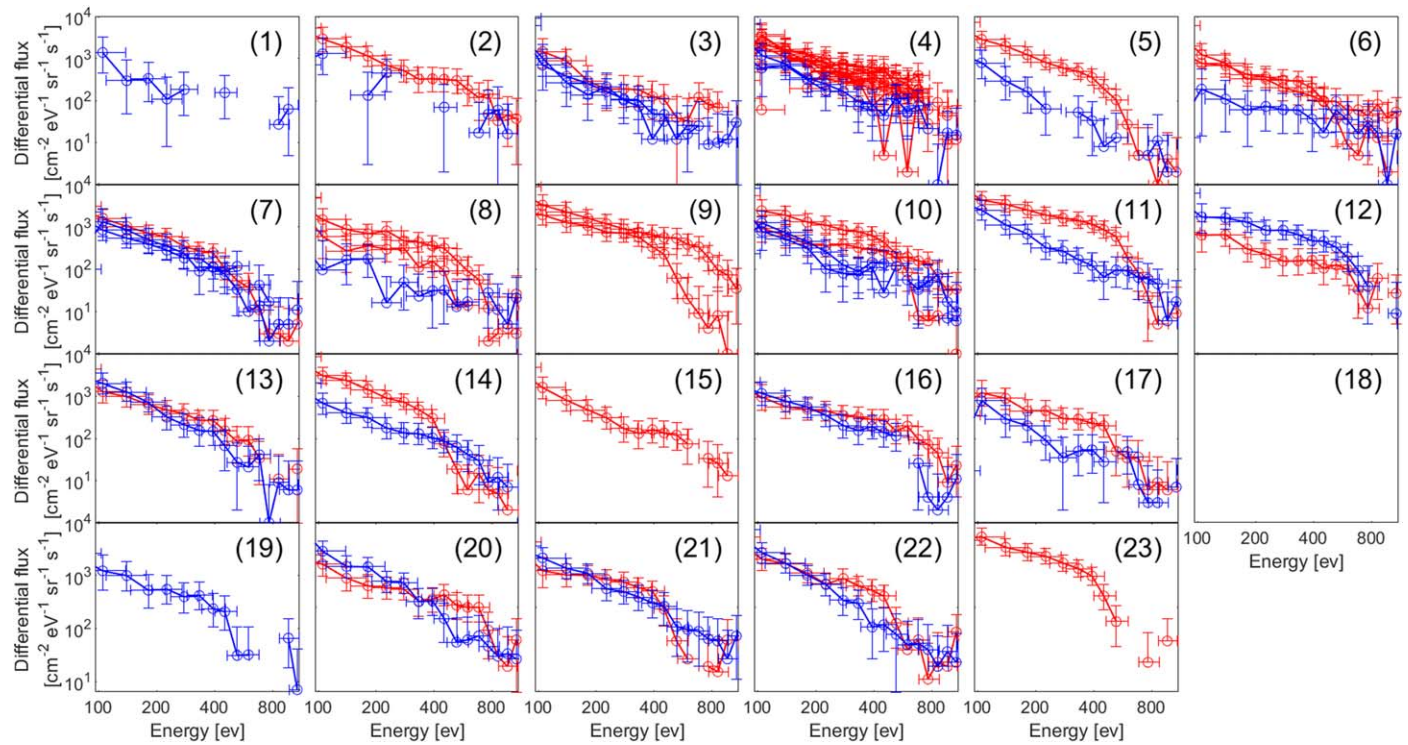
Figure 2. Summary of ASAN ENA spectral distribution over 23 lunar days from 2019/01 to 2020/10. The red and blue lines show the ENA spectral distribution in the lunar dawnside and duskside, respectively. The horizontal error bars indicate the lower and upper limits of the energy bin. The vertical error bars indicate the lower and upper limits of the differential flux. Only data over the sensitivity limit are shown here. The ASAN was powered on aperiodically so that ENAs are not always (e.g., the 1st, 9th, 15th, 19th, and 23rd lunar days) measured at both dawnside and duskside in each lunar day.

105 and 523 eV, up to 0.7 between 140 and 333 eV. The correlation coefficients between the integrated solar wind ion flux and the differential fluxes of ENAs in the E_{ENA}/E_{SW} bin (normalize the measured ENA energy by the solar wind energy) are shown in Figure A3 (we remove the data when the ENA energy is less than 100 eV). We can find that the coefficient on the duskside is relatively larger than those on the dawnside within 0.2–0.9 E_{ENA}/E_{SW} bin, which indicates that the production of ENA in this energy range on the duskside is more directly influenced by the solar wind than that on the dawnside. And c is largest when the ratio of EENA/ESW $\sim$0.1–0.2 (Table A2), which indicates that the protons lose approximately 90% of their initial energy when turned into ENAs during their interaction with the lunar surface. The correlations between the ENA differential flux and the solar wind proton density and dynamic pressure are shown in Figure 4. The ENA differential flux also has a positive correlation with the solar wind density and dynamic pressures in each energy channel. And the correlation coefficient between the ENA differential flux and density is higher on the dawnside. However, the correlation coefficient between the ENA differential flux and dynamic pressure is higher on the duskside. The linear fitting results of Figure 4 are shown in Table A3. The statistics of the relationship between the ENA differential flux and the solar wind velocity are also analyzed with the same method; however, no significant correlation was found (not shown). There is a positive correlation between the solar zenith angle of the rover and the ENA flux/Nsw (ENA flux was normalized by solar wind density), and the correlation coefficient is about 0.4 (Figure A4). The relationship between the solar azimuth angle of the rover and the ENA differential

flux remains unclear because the data are not completely available (not shown).

To quantify the relationship between solar wind energy and ENA energy, we show the relationship between solar wind kinetic energy (determined by the bulk solar wind velocity) and ENA cutoff energy on the dawnside and duskside (Figure 5). The relationship between the ENA temperature (calculation method of Yue et al. 2016 shown in the Appendix) and solar wind kinetic energy on the dawnside and duskside is shown in Figure A5. When calculating the temperature in Figure A5, we excluded several events that might be without a magnetic shielding effect and outside of the lunar mini-magnetosphere or deflected solar wind particles affected by the neighboring magnetic anomalies (Xie et al. 2021). These deflected particles increase the penetration rate to a certain extent that might have an effect on temperature. We show the 95% confidence interval (dashed lines) as error bars of linear fit parameters in Figures 5 and A5. The red lines are relatively higher than the corresponding blue lines in Figures 5 and A5. The calculated ENA temperature is of the same magnitude as the result using the best-fitting parameters for the Maxwell–Boltzmann distribution in Futaana et al. (2012). The blue line shows the linear fitting results on the duskside, and the red line shows the results on the dawnside. The differences between the dawnside and duskside data points in Figures 5 and A5 are statistically significant. This is verified by the t-test applied to the dawn and dusk data sets. The two-sample t-test is a parametric test that can be used to assess whether two samples have the same distribution; a p-value of the t-test of less than 0.05 means that there is a significant statistical difference between the two data sets. The p-values for the cutoff energy and temperature of the two data sets in Figures 5 and A5 are 0.026 and 0.01, respectively, which means
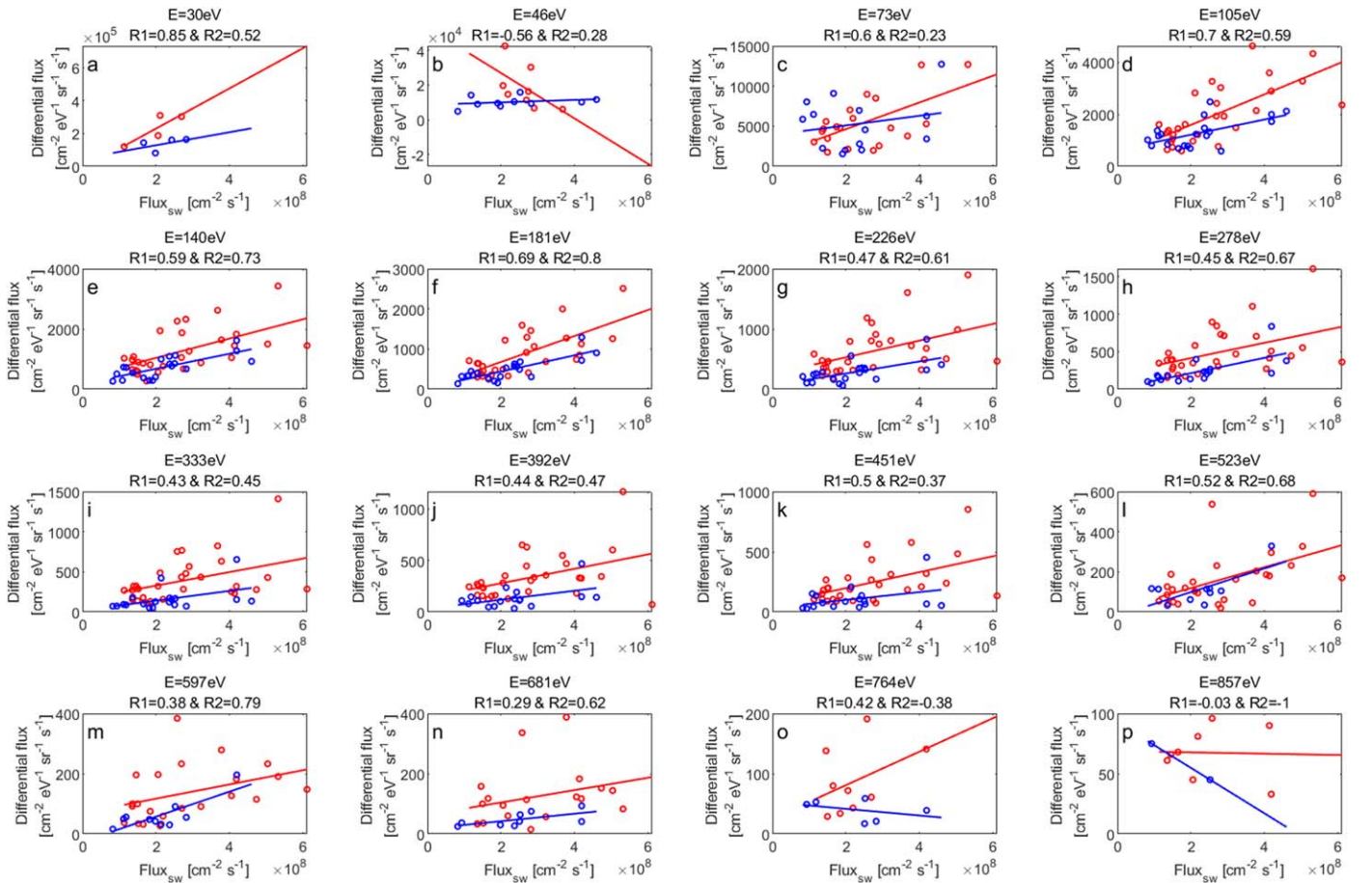
Figure 3. Relationship between the ENA differential flux and solar wind flux at individual energies of ASAN from 30 to 857 eV. The red circles indicate the data on the lunar dawnside, and the blue circles indicate the data on the lunar duskside. Here R1 and R2 represent the correlation coefficients on the dawnside and duskside, respectively. The linear fitting results of the integrated solar wind flux and the ENA differential flux in each ASAN energy bin are shown in Table A1, $df_{ENA} = c^*f_{SW} + k$.

that there is a significant statistical difference between these two data sets. This confirms that the dawnside and duskside data sets belong to two different distributions. We find that the ENA cutoff energy and temperature are lower on the duskside than on the dawnside at the same solar wind energy, which indicates that the solar wind deceleration occurs on the duskside, narrowing the ENA energy spectrum (low temperature) and lowering the ENA cutoff energy.

4. Discussion

The solar wind particle bombardments and compressions of the lunar crustal magnetic field may produce mini-magneto-spheres and possibly bow shocks ahead of the lunar mini-magnetospheres (Lin et al. 1998). Lunar Prospector observations show the presence of an electron cavity at low altitudes over the Crisium, which is the first evidence of the presence of a mini-magnetosphere (Halekas et al. 2008). More recently, the reduction of the ENA flux and reflection of the solar wind protons within the lunar magnetic anomalies further suggest that mini-magnetospheres effectively shield the solar wind plasma (Wieser et al. 2010; Lue et al. 2011; Vorburger et al. 2012; Futaana et al. 2013). The solar wind proton reflection efficiency, largely correlated with crustal magnetic field strength, is 5%–12%, on average, and can be up to 50% of the solar wind flux (Saito et al. 2008; Lue et al. 2011; Poppe et al. 2017). The reduction of the ENA energy exceeding

150 eV within the magnetic anomalies arises from the shielding effect due to solar wind deflection resulting from the mini-magnetosphere (Wieser et al. 2010). This is the first observation of a mini-magnetosphere above a lunar magnetic anomaly using ENA data and shows that the ENA differential flux can be influenced by a mini-magnetosphere.

As shown in Figures 2 and A2, the ENA differential flux is still lower on the duskside, even when the solar wind flux is higher on the duskside. The dawn–dusk asymmetries of the ENA differential flux can be attributed to the shielding effects of the lunar mini-magnetosphere on the duskside, which is supported by 3D magnetohydrodynamic modeling (Xie et al. 2015, 2021). During dawnside measurements, the solar wind comes from northeast of the rover. In this case, the solar wind can bombard the lunar regolith directly, and the backscattered ENA will be detected by the ASAN. However, when the ASAN operates at the lunar duskside, the solar wind from northwest of the rover is most likely to be influenced by the lunar mini-magnetosphere produced by the magnetic anomalies on the northwestern rim of the South Pole-Aitken basin.

In Figures 3 and 4, the measured ENA flux is mainly dependent on solar wind flux, density, and dynamic pressure, which is consistent with the previous observations by Chandrayaan-1 and IBEX (Wieser et al. 2009). The correlation coefficient is higher in energy channels from ∼100 to ∼600 eV, and the peak is from about 140 to 333 eV.
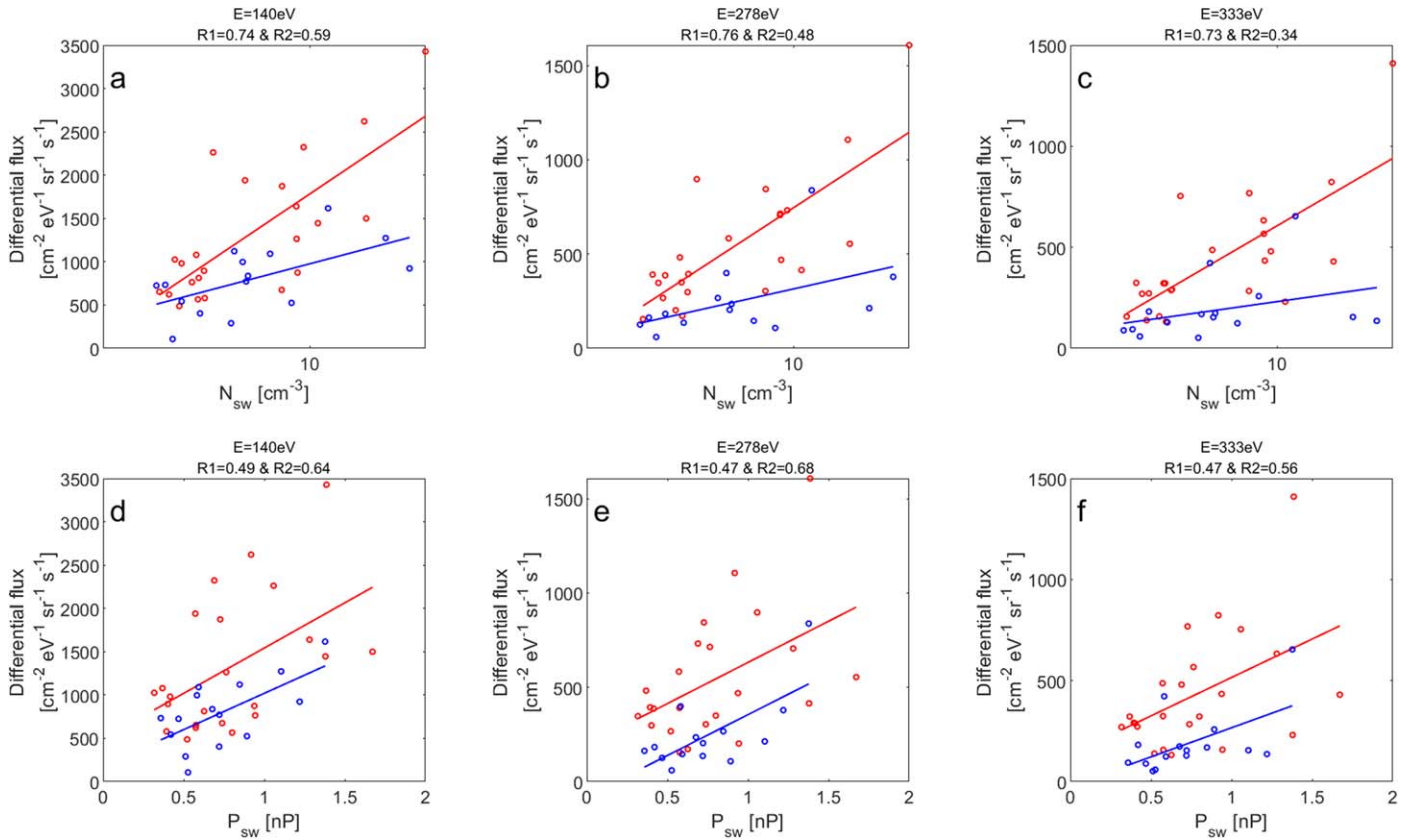
Figure 4. Relationship between the ENA differential flux and solar wind density (a)–(c) and dynamic pressure (d)–(f) at individual ASAN energies. The red circles indicate the data on the lunar dawnside, and the blue circles indicate the data on the lunar duskside. Here R1 and R2 represent the correlation coefficients on the dawnside and duskside, respectively. The linear fitting results of the solar wind density and pressure and the ENA differential flux in each ASAN energy bin are shown in Table A2.

Wieser et al. (2010) found that the mini-magnetosphere is hardly visible in lower-energy hydrogen atoms (<100 eV), whereas it is pronounced in the energy range from 150 to 600 eV. They concluded that this discrepancy shows the presence of two populations of hydrogen atoms that seem to have different origins. One population has lower energies, below 100 eV, while the other exhibits energies larger than 150 eV. The latter population is probably directly related to the impinging solar wind protons because the mini-magnetosphere is visible in images produced from these hydrogen atoms (Wieser et al. 2010). The hydrogen ENA energy spectrum measured by the ASAN agrees well with those measured by Chandrayaan-1 and IBEX above 100 eV, whereas the ASAN data show a higher flux below 100 eV compared with the Chandrayaan-1 and IBEX data (Zhang et al. 2020). It is also proposed that the component above 100 eV mostly consists of solar wind protons directly backscattered as hydrogen ENAs, while below this energy, ENAs sputtered from the surface material become important. The proton ENA flux at energies less than 100 eV may be contaminated by the sputtered ENAs from the lunar surface and the internal surface of the instrument (Wieser et al. 2020; Zhang et al. 2020). The calculated correlation coefficient between the solar wind proton flux observed from ARTEMIS and ENA flux confirms that the ENA energy ranges from 100 to 600 eV originates from solar wind protons, which supports the previous result of Wieser et al. (2010). The origin of fluxes with energies below 100 eV is puzzling and will be investigated in future works. We also examined the relationship between the scattering ratio and the solar wind parameters but found no obvious correlation.

Recent observations by the Kaguya mission at 30 km altitude showed that some magnetic anomalies decelerate and deflect the solar wind ions, which indicates that the large-scale electrostatic potentials form above the lunar magnetic anomalies (Saito et al. 2012). They analyzed a magnetic anomaly in the South Pole-Aitken basin and found that both protons and alpha particles are decelerated by ~150 eV/q (electron volts per unit charge). The creation of ambipolar electric fields over lunar magnetic anomalies has also been reproduced based on particle-in-cell simulations of solar wind interactions with lunar magnetic anomalies (Poppe et al. 2012). Recently, Futaana et al. (2013) found an electrostatic potential larger than $+135$ eV/q inside the Gerasimovic anomaly using the data from the neutral atom energy spectrometer SARA/CENA on board Chandrayaan-1, which is in agreement with the result from the Kaguya observations. This interaction process has also been revealed by numerical simulations using magneto-hydrodynamic, hybrid, and kinetic/particle-in-cell numerical simulations. These simulations indicate that the large-scale ambipolar and/or Hall electrostatic fields may be the primary mechanism of the interaction between the plasma and lunar crustal magnetic fields.

In Figure 5, we find that the ENA cutoff energy and temperature are lower on the duskside than on the dawnside at the same solar wind energy. The solar wind observed by ARTEMIS cannot be influenced by this electrostatic potential above the lunar magnetic anomalies because the interaction
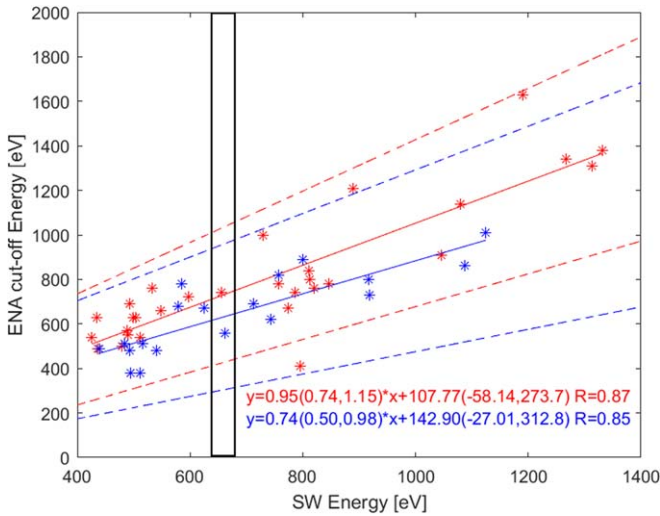
Figure 5. Relationships between solar wind energy and ENA cutoff energy on the dawnside (red line) and duskside (blue line). The dashed lines indicate 95% confidence intervals. The rectangle indicates two events in which the solar wind energy was similar (about 680 eV) on both the dawnside and duskside.

region is most likely located at low altitudes, e.g., $\sim$30 km altitude (Kurata et al. 2005), which is lower than ARTEMIS's orbital altitude. On the duskside, the solar wind might be influenced by the lunar mini-magnetosphere so that the solar wind would be decelerated by the electrostatic potentials above the magnetic anomalies. Therefore, to generate ENAs with the same energy, solar wind protons on the duskside with higher energies are required before their interaction with the surface due to deceleration inside the mini-magnetosphere. The solar wind deceleration on the duskside can be estimated from the difference between the ENA cutoff energy on the dawnside and that on the duskside, and then the electrostatic potential is calculated. The electrostatic potential was estimated by the ENA cutoff energy difference between the dawnside and duskside fitting results (solid red and blue lines in Figure 5). The deceleration rate of the solar wind energy is derived by dividing the ENA cutoff energy difference by the initial solar wind energy, as shown in Figure A6. The 95% confidence interval is also displayed. We can find that the electrostatic potential and deceleration rate both vary with solar wind energy. The potential range is 50–260 V (30–350 V for the 95% confidence interval). The deceleration rate of the solar wind energy is 12%–18% (7.5%–30% for the 95% confidence interval). We compared our results with previous works. Electrostatic potential larger than +135 V inside the Gerasimovic anomaly is confirmed using the ESW-TENA model by Futaana et al. (2012); the differences in the solar wind energy between the outside (525 eV) and inside (390 eV) of the anomaly is 135 eV. The presence of a +150 V electric potential inside the South Pole-Aitken magnetic anomaly was found by Kaguya observations (Figure 5 in Saito et al. 2012), in which case, the initial solar wind energy was about 630 eV (Figure 5 in Saito et al. 2012). The deceleration of the solar wind observed by the Chang'E-4 ASAN is also possibly caused by South Pole-Aitken magnetic anomaly. Fortunately, we find two events with an initial solar wind energy (about 680 eV) similar to the Kaguya observation mentioned above (about 630 eV) on both the dawnside and duskside (marked with the rectangle in Figure 5). The difference in the ENA cutoff energy between the

dawnside (680 eV) and duskside (550 eV) is about 130 eV, which is in agreement with the previous results.

This study confirms that the ENA differential flux at energies between 100 and 600 eV is probably directly related to the impinging solar wind protons, because the lunar mini-magnetosphere is shielding the impinging solar wind on the duskside and results in a lower hydrogen atom flux. Therefore, the correlation coefficient between the solar wind proton flux and the ENA flux is highest in this energy range. Using backscattered ENA data and ARTEMIS data, we also give information on the deceleration of the solar wind protons. The large electric potential produced by charge separation also influences the near-surface environment above the magnetic anomalies, such as lunar swirls and water production (Kramer et al. 2011; Li & Garrick-Bethell 2019). As a new technique, the ENA observation plays an important role in the study of airless bodies' interaction with the plasma environment. More work needs to be done on investigating how lunar materials influence the interaction between the plasma and the surface and its effects on the lunar exosphere.

5. Conclusion and Perspective

Based on the ASAN data obtained from the Chang'E-4 mission, we study the ENA energy spectral distribution on the lunar farside surface and its relationship with solar wind conditions. Major concluding remarks are as follows.

(1) The relationships between the ENA differential flux and solar wind parameters, including solar wind flux, number density, dynamic pressure, and the velocity in individual energy channels, are studied on both the dawnside and duskside. The results show that the measured ENA flux strongly depends on the solar wind density and dynamic pressure, being consistent with the previous observations by Chandrayaan-1 and IBEX. It indicates that a portion of the solar wind ions are backscattered from the surface as ENAs. The correlation coefficients between the ENA differential flux and solar wind integrated flux and dynamic pressure are higher on the duskside than on the dawnside. However, a correlation between the measured ENA flux and solar wind velocity cannot be excluded at this stage.

(2) The relationship between the solar wind energy and ENA energy on the dawnside and duskside shows that the production of ENAs with the same energy requires a higher solar wind energy on the duskside, indicating the solar wind may be decelerated by ambipolar and Hall electrostatic fields within a lunar mini-magnetosphere.

Appendix

A.1. The Definition of Angles

The solar azimuth angle is the angle between the projection of the solar direction in the tangent plane at the rover location and the north direction. The value is positive for the clockwise direction, and the range is from $-180°$ to $180°$.

The solar azimuth angle is the angle between the solar direction and the normal of the lunar surface at the rover location, and the range is from $0°$ to $90°$. The solar elevation angle is the complement angle of the solar azimuth angle.

The rover coordinate system is defined as follows. The origin is the center of the baseplate of the rover structure. The X-axis is in the baseplate, and $+X$ points in the direction of the mast installation (the forward direction). The Z-axis is along the normal of the baseplate, and $+Z$ points to the lunar surface. The Y-, Z-, and X-axes form a right-hand coordinate system.

The solar azimuth angle of the rover is the angle between the projection of the solar direction in the X–Y plane of the rover coordinate system and the rover $+X$ direction. The value is positive for the clockwise direction, and the range is from $-180°$ to $180°$.

The solar elevation angle of the rover is the complement angle between the solar direction and the $-Z$ direction of the rover coordinate system, and the range is from $0°$ to $90°$.

A.2. Calculation Method of ENA Temperature

Considering relativistic effects, the particle phase-space density (f) is calculated using the differential energy flux (j) as

$$f = \frac{\gamma^3 m_0 j}{v^2}, \text{ or } f\,[s^3/m^6]$$

$$= 6.25 \times 10^{16} \gamma^3 \frac{m_0[kg]\,j[cm^{-2}MeV^{-1}s^{-1}sr^{-1}]}{v^2[m/s]}, \quad (A1)$$

where γ is the relativistic factor, m_0 is the particle's rest mass, and v is the velocity.

Table A1
The Linear Fitting Results of the Integrated Solar Wind Flux and the Differential Flux in Each ASAN Energy Bin, $df_{ENA} = c^* f_{SW} + k$

E (eV)	dawn_c	dawn_k	dawn_r^2	dusk_c	dusk_k	dusk_r^2
30	1.22E-03	−1.44E+04	0.73	1.29E-04	1.15E+05	0.04
46	−1.31E-04	5.31E+04	0.32	−8.38E-06	1.73E+04	0.00
73	1.66E-05	1.32E+03	0.36	5.98E-06	3.90E+03	0.05
105	5.85E-06	4.20E+02	0.49	2.91E-06	6.36E+02	0.34
140	3.17E-06	3.97E+02	0.34	2.73E-06	9.51E+01	0.55
181	3.20E-06	3.24E+01	0.48	2.09E-06	1.12E+00	0.62
226	1.37E-06	2.51E+02	0.22	1.02E-06	5.89E+01	0.36
278	1.04E-06	2.12E+02	0.20	1.08E-06	−1.24E+01	0.48
333	8.43E-07	1.60E+02	0.18	6.24E-07	1.39E+01	0.22
392	7.02E-07	1.38E+02	0.19	4.59E-07	2.27E+01	0.24
451	6.60E-07	6.64E+01	0.25	3.43E-07	2.76E+01	0.16
523	5.31E-07	1.73E+01	0.27	5.94E-07	−2.07E+01	0.48
597	2.36E-07	6.98E+01	0.15	4.14E-07	−2.53E+01	0.64
681	2.09E-07	6.41E+01	0.08	1.24E-07	1.74E+01	0.39
764	2.78E-07	2.54E+01	0.18	−2.72E-08	4.38E+01	0.04
857	−5.46E-09	6.88E+01	0.00	−1.85E-07	9.30E+01	0.98

Table A2
The Linear Fitting Results of the Integrated Solar Wind Flux and the Differential Flux in Each Ratio of E_{ENA}/E_{SW}, $df_{ENA} = c^* f_{SW} + k$

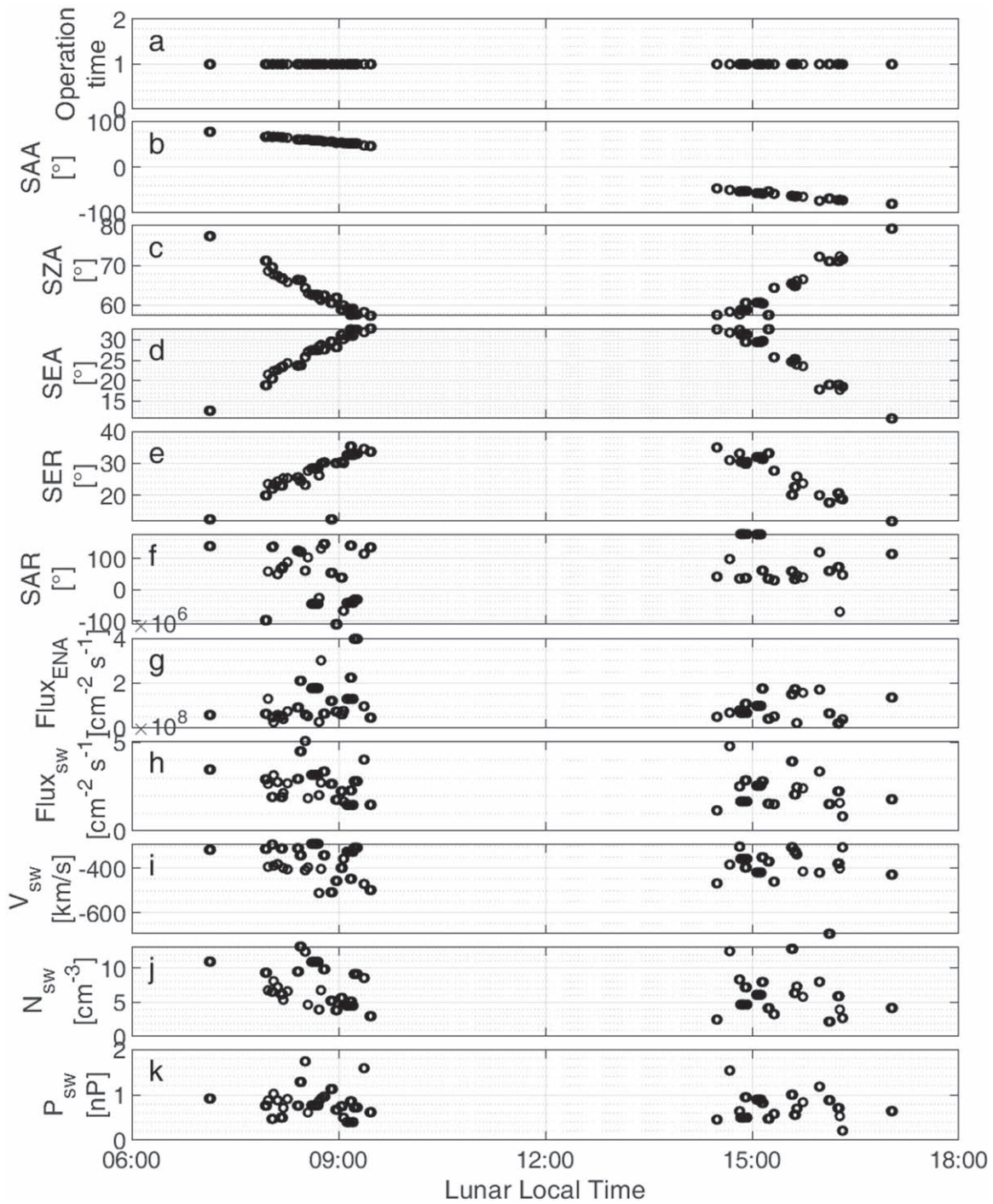| Eena/Esw	dawn_c	dawn_k	dawn_r^2	dusk_c	dusk_k	dusk_r^2
0.1–0.2	1.15E-05	−14.57	0.55	7.15E-06	274.61	0.53
0.2–0.3	4.65E-06	550.53	0.07	6.26E-06	36.65	0.39
0.3–0.4	3.45E-06	278.35	0.09	4.07E-06	−51.68	0.52
0.4–0.5	2.48E-06	234.17	0.09	2.17E-06	3.89	0.38
0.5–0.6	2.21E-06	171.93	0.11	1.63E-06	3.11	0.48
0.6–0.7	1.58E-06	147.30	0.09	9.75E-07	20.68	0.25
0.7–0.8	1.44E-06	85.77	0.10	6.40E-07	31.85	0.35
0.8–0.9	1.25E-06	35.85	0.16	6.01E-07	15.73	0.27

Figure A1. Overview of ASAN geometries and ARTEMIS data: (a) ASAN operation times, (b) solar azimuth angle, (c) solar zenith angle, (d) solar elevation angle, (e) solar elevation angle of rover, (f) solar azimuth angle of rover, (g) ENA flux, (h) solar wind flux, (i) solar wind velocity, (j) solar wind density, and (k) solar wind dynamic pressure as a function of the lunar local time.

Table A3
The Linear Fitting Results of the Integrated Solar Wind Density and Pressure and the Differential Flux in Each ASAN Energy Bin

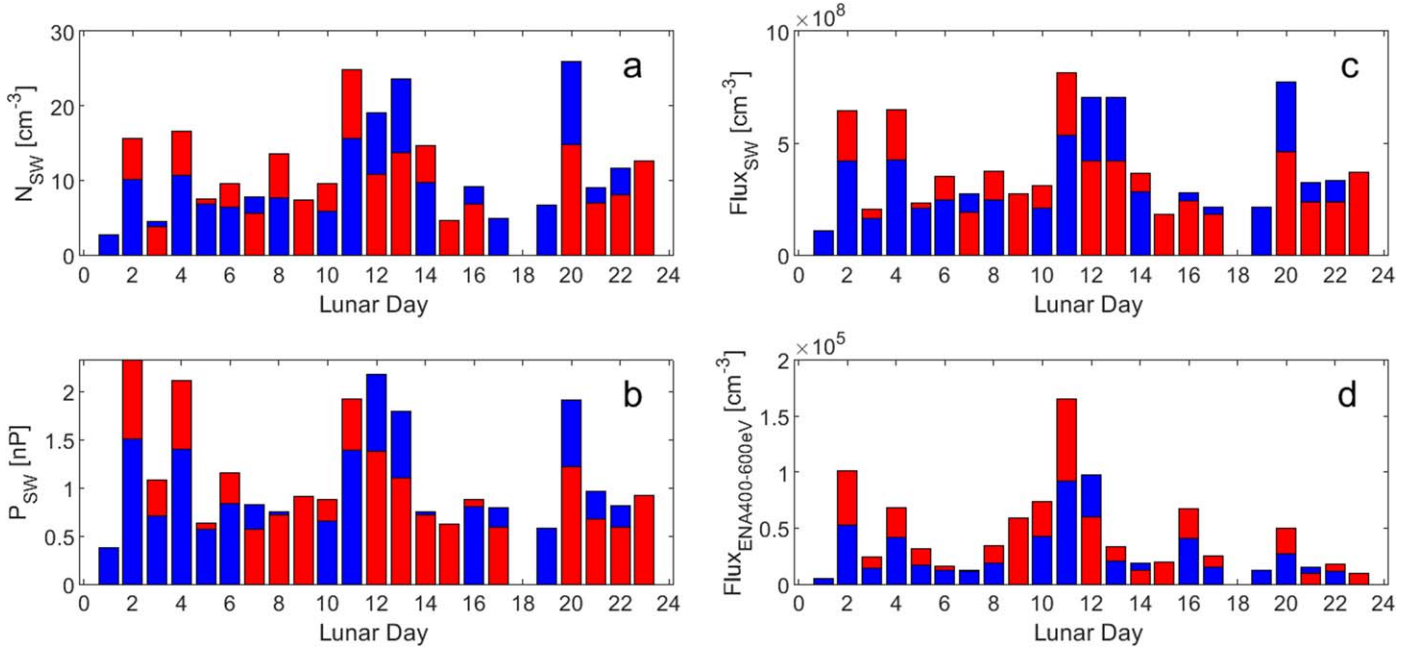|	E (eV)	dawn_c	dawn_k	dawn_r^2	dusk_c	dusk_k	dusk_r^2
	140	1.65E+02	90.38	0.53	4.93E+01	396.71	0.24
Density	278	7.14E+01	35.12	0.57	1.75E+01	81.18	0.12
	333	6.06E+01	−0.66	0.54	7.52E+00	111.52	0.03
	140	1.15E+03	364.86	0.28	8.12E+02	177.03	0.38
Pressure	278	4.31E+02	204.21	0.22	4.32E+02	−103.58	0.43
	333	3.91E+02	123.76	0.24	2.75E+02	−33.36	0.26

9

Figure A2. Overview of the ASAN geometries and solar wind parameters over 23 lunar days. (a)–(b) Solar wind density and pressure. (c)–(d) Solar wind flux and ENA flux with 200–600 eV. The red bars indicate the mean data on the dawnside of the Moon, and the blue bars indicate the mean data on the duskside of the Moon.
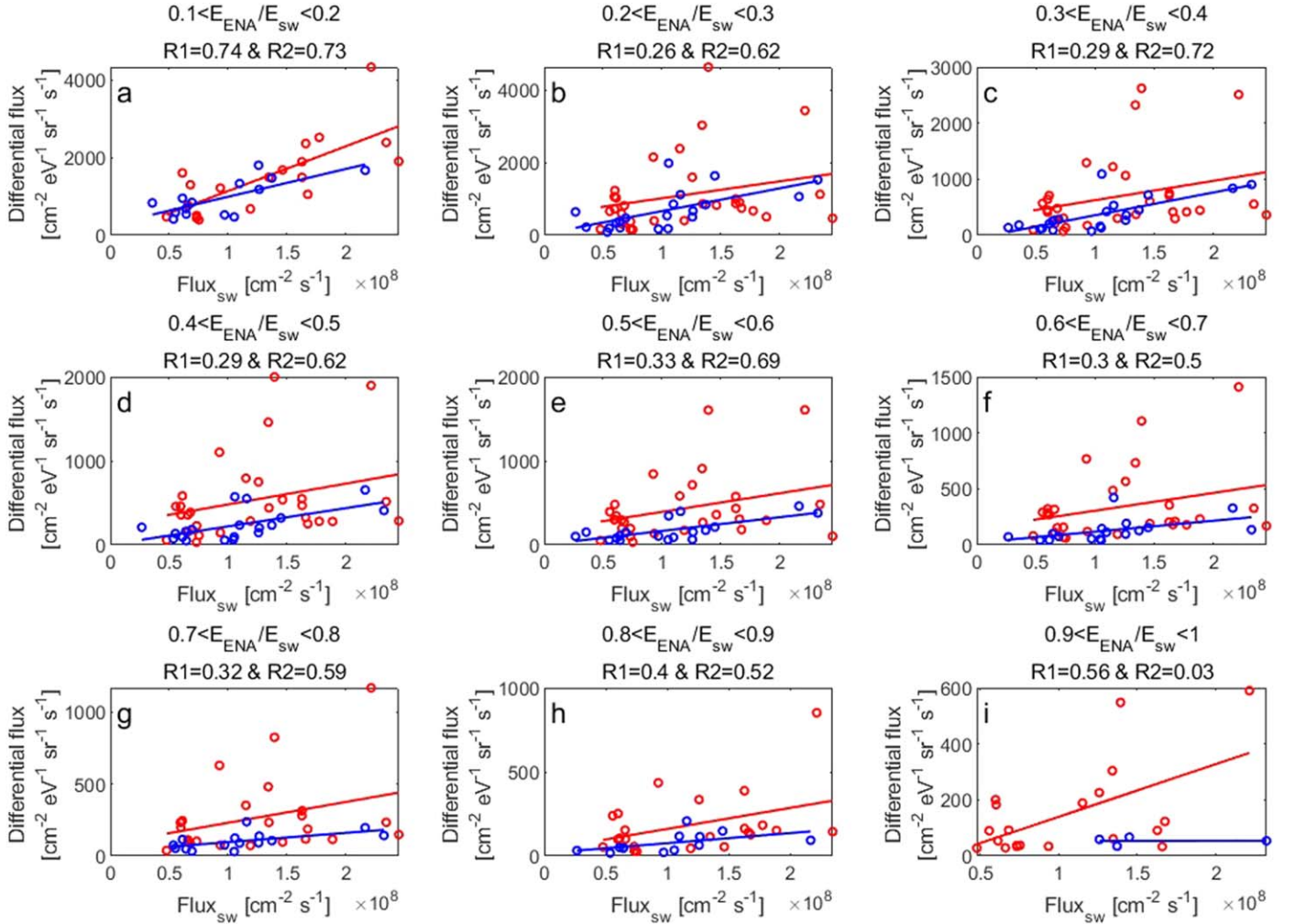

Figure A3. Correlation coefficients between the integrated solar wind ion flux and the differential fluxes of ENAs in the E_{ENA}/E_{SW} bin (normalize the measured ENA energy by the solar wind energy). The red and blue lines show the results on the dawnside and duskside, respectively. Here R1 and R2 represent the correlation coefficients on the dawnside and duskside, respectively.
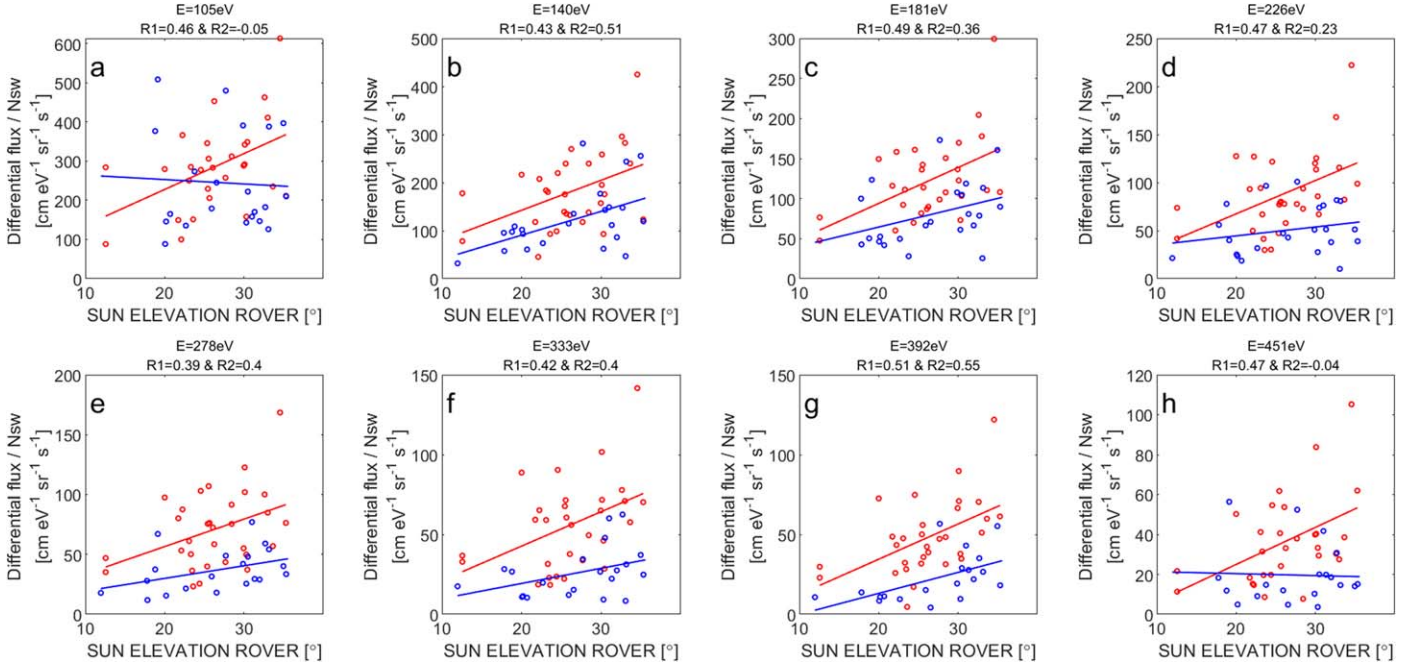
Figure A4. Relationship between the ENA differential flux/Nsw and the solar elevation angle of the rover at an individual energy of ASAN from 105 to 451 eV. The red circles indicate the data on the lunar dawnside, and the blue circles indicate the data on the lunar duskside. Here R1 and R2 represent the correlation coefficients on the dawnside and duskside, respectively.
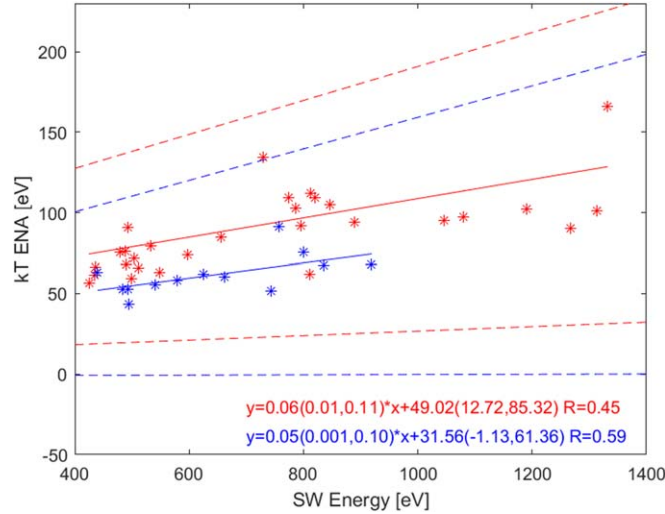

Figure A5. Relationships between solar wind energy and ENA absolute temperature on the dawnside (red line) and duskside (blue line). The dashed lines are 95% confidence intervals.

The γ and v are calculated using the relations

$$E_k = (\gamma - 1)m_0 c^2 \quad \text{and} \quad \frac{v^2}{c^2} = 1 - \frac{1}{\left(\frac{E_k}{m_0 c^2} + 1\right)^2}, \quad \text{(A2)}$$

where c is the light speed and E_k is the particle's kinetic energy.

The integrated particle density is calculated as

$$n = \int_{v_{\min}}^{v_{\max}} \int_0^\pi 2\pi \sin(\alpha) v^2 f d\alpha dv, \quad \text{(A3)}$$

where α is the pitch angle.

The parallel and perpendicular pressures are calculated as

$$P_\parallel = \int_{v_{\min}}^{v_{\max}} \int_0^\pi 2\pi \sin(\alpha)\cos^2(\alpha) m_0 v^4 f d\alpha dv \quad \text{(A4)}$$

and

$$P_\perp = \int_{v_{\min}}^{v_{\max}} \int_0^\pi \pi \sin^3(\alpha) m_0 v^4 f d\alpha dv. \quad \text{(A5)}$$

The temperature is calculated as

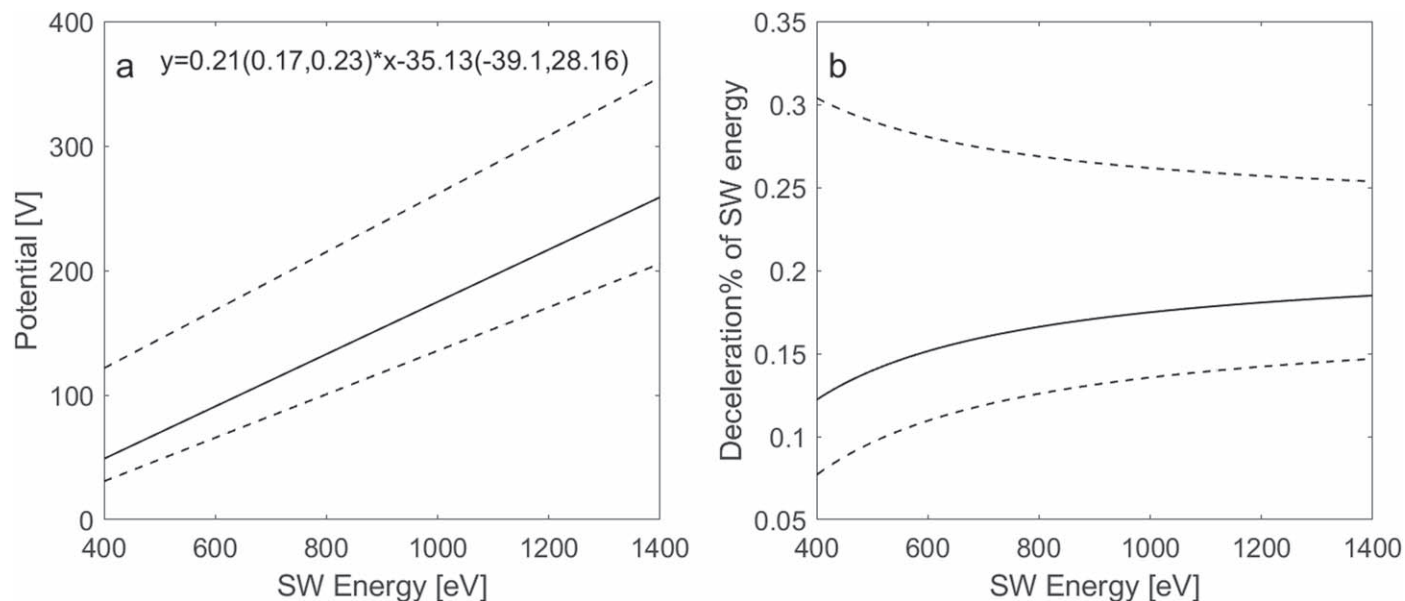$$T = P/n\text{K}. \quad \text{(A6)}$$

11

Figure A6. The possible solar wind electrostatic potential and deceleration percentage of the solar wind are derived from Figure 5. The dashed lines are 95% confidence intervals.

ORCID iDs

H. Z. Wang ⓘ https://orcid.org/0000-0002-3652-6210
C. Xiao ⓘ https://orcid.org/0000-0002-2633-9526
Q. Q. Shi ⓘ https://orcid.org/0000-0001-6835-4751
R. L. Guo ⓘ https://orcid.org/0000-0002-7125-0942
C. Yue ⓘ https://orcid.org/0000-0001-9720-5210
L. H. Xie ⓘ https://orcid.org/0000-0001-9635-4644
J. Zhang ⓘ https://orcid.org/0000-0002-8369-871X
M. Wieser ⓘ https://orcid.org/0000-0002-1760-210X
Y. Saito ⓘ https://orcid.org/0000-0002-1354-3544
M. N. Nishino ⓘ https://orcid.org/0000-0001-5992-445X
M. Nowada ⓘ https://orcid.org/0000-0003-4849-3433
Q. G. Zong ⓘ https://orcid.org/0000-0002-6414-3794
A. M. Tian ⓘ https://orcid.org/0000-0002-4351-551X
H. Zhang ⓘ https://orcid.org/0000-0002-3680-4989
J. Chen ⓘ https://orcid.org/0000-0003-3759-0254
T. X. Zhang ⓘ https://orcid.org/0000-0001-5535-2976
J. Liu ⓘ https://orcid.org/0000-0001-6648-8908
W. S. Shang ⓘ https://orcid.org/0000-0002-7078-8249

References

Allegrini, F., Dayeh, M. A., Desai, M. I., et al. 2013, P&SS, 85, 232
Angelopoulos, V. 2011, SSRv, 165, 3
Crider, D. H., & Vondrak, R. R. 2002, AdSpR, 30, 1869
Di, K., Liu, Z., Liu, B., et al. 2019, JRemS, 23, 177
Fairfield, D. H. 1971, JGR, 76, 6700
Funsten, H. O., Allegrini, F., Bochsler, P. A., et al. 2013, JGRE, 118, 292
Futaana, Y., Barabash, S., Holmström, M., & Bhardwaj, A. 2006, P&SS, 54, 132
Futaana, Y., Barabash, S., Wieser, M., et al. 2012, JGR, 117, E05005
Futaana, Y., Barabash, S., Wieser, M., et al. 2013, GeoRL, 40, 262
Halekas, J. S., Delory, G. T., Brain, D. A., Lin, R. P., & Mitchell, D. L. 2008, P&SS, 56, 941
Harada, Y., Futaana, Y., Barabash, S., et al. 2014, JGRA, 119, 3573
Kramer, G. Y., Besse, S., Dhingra, D., et al. 2011, JGR, 116, E00G18
Kurata, M., Tsunakawa, H., Saito, Y., et al. 2005, GeoRL, 32, L24205
Li, S., & Garrick-Bethell, I. 2019, GeoRL, 46, 14318
Lin, R. P., Mitchell, D. L., Curtis, D. W., et al. 1998, Sci, 281, 1480
Liu, J., Ren, X., Yan, W., et al. 2019, NatCo, 10, 4229
Liu, Z., Di, K., Li, J., et al. 2020, Sci. China Inf.. Sci, 63, 140901
Lue, C., Futaana, Y., Barabash, S., et al. 2011, GeoRL, 38, L03202
Lue, C., Futaana, Y., Barabash, S., et al. 2016, JGRA, 121, 432
McComas, D. J., Allegrini, F., Bochsler, P., et al. 2009, GeoRL, 36, L12104
McFadden, J. P., Carlson, C. W., Larson, D., et al. 2008, SSRv, 141, 277
Poppe, A. R., Halekas, J. S., Delory, G. T., & Farrell, W. M. 2012, JGR, 117, A09105
Poppe, A. R., Halekas, J. S., Lue, C., & Fatemi, S. 2017, JGRE, 122, 771
Saito, M. H., Miyashita, Y., Fujimoto, M., et al. 2008, GeoRL, 35, L07103
Saito, Y., Yokota, S., Asamura, K., et al. 2010, SSRv, 154, 265
Saito, Y., Nishino, M. N., Fujimoto, M., et al. 2012, EP&S, 64, 83
Schaufelberger, A., Wurz, P., Barabash, S., et al. 2011, GeoRL, 38, L22202
Sibeck, D. G., Angelopoulos, V., Brain, D. A., et al. 2011, SSRv, 165, 59
Shue, J. -H., Chao, J. K., Fu, H. C., et al. 1997, JGR, 102, 9497
Vorburger, A., Wurz, P., Barabash, S., et al. 2012, JGRA, 117, A07208
Vorburger, A., Wurz, P., Barabash, S., et al. 2013, JGRA, 118, 3937
Vorburger, A., Wurz, P., Barabash, S., et al. 2015, P&SS, 115, 57
Wang, H. Z., Zhang, J., Shi, Q. Q., et al. 2021, ApJL, 907, L32
Wang, X. -D., Bian, W., Wang, J. -S., et al. 2010, GeoRL, 37, L07203
Wieser, M., Barabash, S., Futaana, Y., et al. 2009, P&SS, 57, 2132
Wieser, M., Barabash, S., Futaana, Y., et al. 2010, GeoRL, 37, L05103
Wieser, M., Barabash, S., Wang, X. -D., et al. 2020, SSRv, 216, 73
Wu, W., Li, C., Zuo, W., et al. 2019, NatGe, 12, 222
Xie, L., Li, L., Zhang, A., et al. 2021, GeoRL, 48, e93943
Xie, L., Li, L., Zhang, Y., et al. 2015, JGRA, 120, 6559
Yue, C., An, X., Bortnik, J., et al. 2016, GeoRL, 43, 7804
Zhang, A., Wieser, M., Wang, C., et al. 2020, P&SS, 189, 104970